Numerical prediction of hydrodynamic coefficients for a semi-sub platform by using large eddy simulation with volume of fluid method and Richardson extrapolation

IOP Conf. Series: Journal of Physics: Conf. Series **1356** (2019) 012034 doi:10.1088/1742-6596/1356/1/012034

Numerical prediction of hydrodynamic coefficients for a semi-sub platform by using large eddy simulation with volume of fluid method and Richardson extrapolation

Jia Pan[1], **Takeshi Ishihara**[1]

[1] *Department of Civil Engineering, School of Engineering, The University of Tokyo, Japan,7-3-1 Hongo, Bunkyo, 113-8656 Tokyo, Japan*

E-mail: ishihara@bridge.t.u-tokyo.ac.jp

Abstract. Hydrodynamic coefficients for predicting hydrodynamic loading is significant for the design of offshore wind turbine floaters. In this paper, hydrodynamic coefficients for a semi-submersible floating offshore wind turbine are investigated experimentally and numerically. In the water tank test, added mass and drag coefficients of the semi-submersible model are identified by the forced oscillation tests. In numerical simulation, large eddy simulation (LES) with volume of fluid method (VOF) is adopted to predict added mass and drag coefficients. Firstly, numerical errors in the predicted hydrodynamic coefficients are systematically studied, and Richardson extrapolation is employed to obtain the grid independent solution. The predicted added mass and drag coefficients varying with KC number are then validated by the water tank tests and the mechanism of the hydrodynamic force are clarified by vortex shedding patterns. The hydrodynamic coefficients for each element are also investigated. Finally, effect of free surface on the hydrodynamic forces is discussed and the predicted added mass and drag coefficients are compared with those obtained from the water tank tests.

1. Introduction

Floating offshore wind turbine (FOWT) is a promising innovation for generating electricity from renewable energy. Comparing with other types of floaters, the semi-submersible type of FOWT containing columns, heave plates, pontoons and braces, is one of the most complex types and received main attention, as there are some advantages such as the high adaptedness for both shallow and deep water, and the competitive cost. In WindFloat project [1], a 2MW FOWT with a semi-submersible foundation was installed in 2011. In Japan, a 2MW compact semi-submersible FOWT and a 7MW V-shape semi-submersible FOWT have been constructed and operated in Fukushima Project [2]. The platforms are set in the sea states where the wave period is near to the natural period of floater motion, so hydrodynamic coefficients for predicting nonlinear hydrodynamic loading by Morison's equation [3] and potential theory [4] is significant for the design of FOWTs.

A number of numerical studies on the hydrodynamic coefficients has been conducted for simple heave plates or cylinders, and compared with the water tank tests by Tao et al.[5], [6], [7]. Lopez-Pavon and Souto-Iglesias [8] predicted the hydrodynamic coefficients for a heave plate by RANS model, and provided reasonable results for plain plate, but there were some errors for reinforced plate.

Benitz et al. [9] predicted the hydrodynamic coefficients for the simplified OC4-DeepWind semi-submersible, and highlighted the role of free surface in the fluid flow near the structure. Zhang and Ishihara [10] investigated the hydrodynamic coefficients of multiple heave plates by large eddy simulation (LES) turbulent model with volume of fluid (VOF) method and the numerical results matched well with the experimental data. Unlike a simple plate, numerical prediction of hydrodynamic coefficients for a semi-submersible platform by CFD is a challenge due to the complexity of platform and interaction between the elements. It is difficult to obtain the cost-effective and reliable solution by refining grid only, the methodology to provide an accurate solution is necessary. Furthermore, systemic research of free surface on the hydrodynamic coefficients in the horizontal and vertical directions has not been conducted.

Klaka et al. [11] indicated that the hydrodynamic coefficients strongly depend on Keulegan Carpenter (KC) number [12], and the added mass coefficients predicted by the potential theory were not accurate comparing with the experimental data. However, dependency of hydrodynamic coefficients on KC number for a semi-submersible platform has not been discussed, and the distribution of hydrodynamic coefficients has not been investigated yet.

Section 2 describes the numerical model used in this study, including the model description, governing equations, numerical setup and water tank tests. In Section 3, numerical errors in the predicted hydrodynamic coefficients based on three levels of grid are systematically studied. The grid independent solution by Richardson extrapolation is investigated and validated by the experiment. The dependency of added mass and drag coefficients on KC number are then numerically examined and compared with the water tank test. The distribution of hydrodynamic coefficients for each element is also investigated. Finally, effects of free surface on the added mass and drag coefficients are discussed and compared with those from the water tank tests. Conclusions are summarized in Section 4.

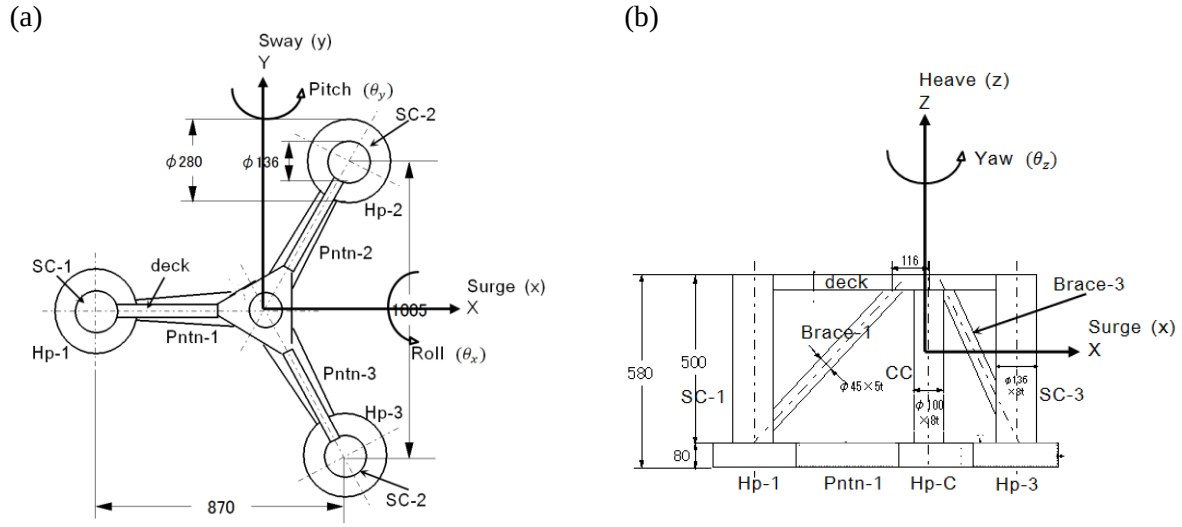

Fig. 1. (a) Top view and (b) side view of the model and their dimensions, units (mm).

2. Numerical model

Numerical model of a down-scaled semi-submersible floating platform is described in section 2.1. The governing equation by using LES with VOF method are introduced in section 2.2 and computational domain including the grid system used in the numerical simulation is described in section 2.3. Numerical schemes and boundary conditions are presented in section 2.4. The definition of the hydrodynamic coefficients is provided in section 2.5 and the water tank test is described in section 2.6.

2.1 Model description

A 1/50 down-scaled semi-submersible type of platform based on the 2MW floating offshore wind turbine system in Fukushima Forward Project is used in the water tank tests and numerical simulations. The floater contains four columns connected by three pontoons, three braces and three decks. The overview of the floater and its dimensions are shown in Table 1. The total weight of the platform model is 42.2 kg and the model draft is 0.38m as shown in the reference [13]. A summary of the geometry, including diameter and height for each element is illustrated in the Table 1, and the characteristic volume and area of elements in the vertical and horizontal directions for normalizing hydrodynamic coefficients in this study are listed in Table 2.

Table 1. Specifications of the 1/50 scaled model geometry of the FOWT model.

Elements	Dimension (m)
Total draft of the platform	0.38
Elevation of center column(tower base) and side columns(SC) above SWL	0.2
Spacing between side columns	1.005
Height of center columns (CC) and side columns	0.5
Diameter of center column	0.1
Diameter of side columns	0.136
Depth to top of heave plates(Hp) below SWL	0.3
Height of heave plates and pontoon (Pntn)	0.08
Diameter of heave plate	0.28
Width of pontoon	0.06~0.12
Length of pontoon	0.39
Diameter of brace (Brace)	0.045
Height of deck	0.045
Width of deck	0.045
Center of gravity below SWL	-0.166
meta-centric height above SWL	0.086
Radius of gyration K_{xx}	0.52
Radius of gyration K_{yy}	0.51

Table 2. Characteristic volume and area of each element in the vertical and horizontal directions for normalizing hydrodynamic coefficients of 1/50 scaled model.

	Volume (m^3)	Area in horizontal (m^2)	Area in vertical (m^2)	Area of water plane (m^2)
Side column SC-1	0.004358	0.0408	0	0.014527
Side column SC-2	0.004358	0.0408	0	0.014527
Side column SC-3	0.004358	0.0408	0	0.014527
Center column Cc	0.002356	0.03	0	0.007854
Heave plate Hp-1	0.004926	0.0224	0.061575	0
Heave plate Hp-2	0.004926	0.0224	0.061575	0
Heave plate Hp-3	0.004926	0.0224	0.061575	0
Center heave plate Hp-C	0.002993	0.0192	0.037412	0
Pontoon Pntn-1	0.002433	0.030409	0.0269	0
Pontoon Pntn-2	0.002433	0.030409	0.0269	0
Pontoon Pntn-3	0.002433	0.030409	0.0269	0
Brace Br-1	0.000524	0.014764	0	0.002249
Brace Br-2	0.000524	0.014764	0	0.002249
Brace Br-3	0.000524	0.014764	0	0.002249
Total value [13]	0.04219	0.3216	0.185	0.058182

2.2 Governing equation

Large-eddy simulation (LES) is adopted in this study The Boussinesq hypothesis is employed, and the standard Smagorinsky-Lilly model is used to calculate the subgrid-scale stresses. The governing equations in Cartesian coordinates are expressed in the form of tensor as

$$\frac{\partial \tilde{u}_i}{\partial x_i} = 0 \tag{1}$$

$$\rho \frac{\partial \tilde{u}_i}{\partial t} + \rho \frac{\partial \tilde{u}_i \tilde{u}_j}{\partial x_j} = -\frac{\partial \tilde{p}}{\partial x_i} + \frac{\partial}{\partial x_j}\left[\mu\left(\frac{\partial \tilde{u}_i}{\partial x_j} + \frac{\partial \tilde{u}_j}{\partial x_i}\right)\right] - \frac{\partial \tau_{ij}}{\partial x_j} \tag{2}$$

where $\tilde{u}_i$ and $\tilde{p}$ are the filtered velocity and pressure, respectively. μ is the molecular viscosity, and ρ is the density of fluid. $\tau_{ij} = \rho\ u_i u_j - \tilde{u}_i \tilde{u}_j$ is the subgrid-scale stress resulting from the filtering operations, and is expressed as

$$\tau_{ij} = -2\mu_t \tilde{S}_{ij} + \frac{1}{3}\tau_{ii}\delta_{ij} \tag{3}$$

In which, μ_t is the subgrid-scale turbulent viscosity, and $\tilde{S}_{ij}$ is the rate-of –strain tensor for the resolved scale defined as

$$\tilde{S}_{ij} = \frac{1}{2}\left(\frac{\partial \tilde{u}_i}{\partial x_j} + \frac{\partial \tilde{u}_j}{\partial x_i}\right) \tag{4}$$

Smagorinsky-Lilly model is used to calculate the subgrid-scale turbulent viscosity, μ_t defined as

$$\mu_t = \rho L_S^2 \left|\tilde{S}\right| = \rho L_S \sqrt{2\tilde{S}_{ij}\tilde{S}_{ij}} \tag{5}$$

where, L_S is the mixing length for subgrid-scales, defined as

$$L_S = \min\left(\kappa\delta, C_s V^{1/3}\right) \tag{6}$$

In which, κ is the von Karman constant, 0.42, C_s is Smagorinsky constant and is set as 0.032 following the suggestion in the reference [14], δ is the distance to the closest wall and V is the volume of a computational cell.

Volume of Fluid (VOF) model is used to model air and water and to capture interface between air and water. Volume fraction of water will be solved to capture the interface between water and air. Continuity equation for the volume fraction of water α_w is expressed as

$$\frac{1}{\rho_w}\left[\frac{\partial}{\partial t}\left(\alpha_w \rho_w\right) + \nabla\left(\alpha_w \rho_w \vec{v}_w\right)\right] = 0 \tag{7}$$

where ρ_w is water density.

2.3 Computational domain and grid arrangement

The numerical setup of simulation follows the water tank test. The whole computational domain and grid around the model are displayed in Fig. 2. The computational domain is divided into two subdomains with respect to the simulated phases. The lower subdomain is used to simulate the phase of water and bottom of the subdomain is 4.1h away from the still water level (SWL), where h is the model height of 0.5m. The upper subdomain is utilized to consider the phase of air and top of the subdomain is 1.3h above the SWL. In order to mitigate the reflecting flow from the boundary, side walls are located sufficiently far away from the model. The distance between the model and inlet and outlet is the same value of 20.7h. Hexahedral meshes are used for the whole computational domain except for the region near the center column, where hybrid meshes are employed.

Quality of grid plays a crucial role in the accuracy of numerical results. Grid independences are studied to choose a reasonable grid system. In this study, three different levels of grid system are employed as shown in Table 3. The grids are refined at the locations where the substantial flow separations are expected. As discussed in section 3, the grids are refined near the heave plates and center heave plate since they mostly contribute to the hydrodynamic forces in the vertical direction. The area of 5cm around the heave plates and center heave plate is chosen to be refined considering the vortex shedding. The grids are also refined in the area of 5cm close to the side columns and center column because they play an important role in the hydrodynamic forces in the horizontal direction.

For LES turbulent model, the first layer of mesh near the model is significant, thus more grid points are designed in the boundary layer. In order to refine cells in the selected zones, the heave plates and center heave plate are selected for the boundary adaption during the vertically forced vibration, while the side columns and center column are marked during the horizontally forced vibration. An example of grid refinement with the boundary adaption near the heave plate HP-1 in the vertical direction and the side column SC-1 in the horizontal direction are shown in Fig. 3 and Fig. 4, respectively, in which the number of grid is increased from 13.7 million to 18.8 million. The grids are refined twice by the same regulation, and the grid number of level 3 reaches 63.8 million as shown in Table 3. It is noticed that the number of grid increases rapidly as the grid size decreases. The gird information are summarized in Table. 4. The grid size of first layer in the vertical and radial directions are 1.3 mm and 2 mm, respectively. The grid size is 8 mm for the grid level 1 and 2 mm for the grid level 3 with the expanding factor from 1.0 to 1.2.

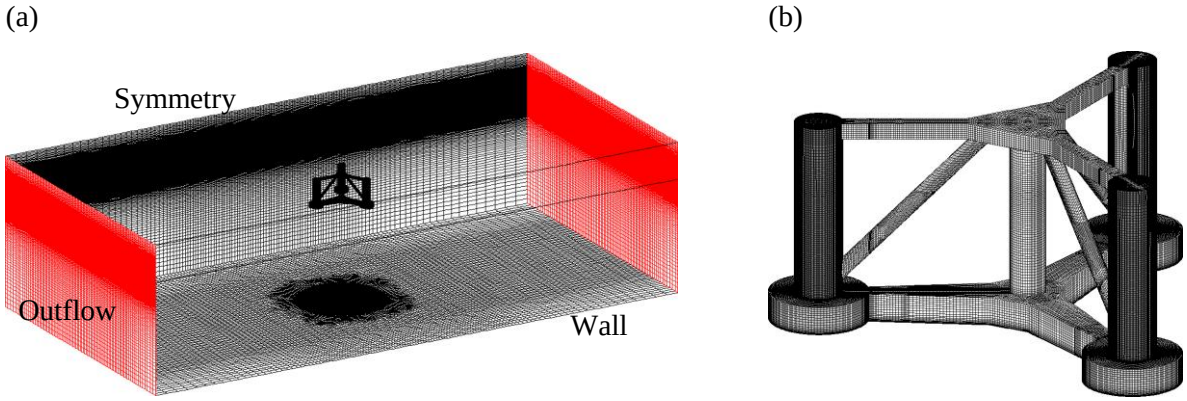

Fig. 2. (a) Computational domain and (b) grid around the model.

Table 3. Description of grid size and grid number for three different grid levels.

Grid level	1	2	3
Grid size	$h_1 = 8\text{mm}$	$h_2 = 4\text{mm}$	$h_3 = 2\text{mm}$
Grid number (million)	13.7	18.8	63.8

Table 4. Summary of grid information.

Parameters	Value
First layer in the radial direction (mm)	2
First layer in the vertical direction (mm)	1.3
Grid size (mm)	2~8
Expanding factor	1.0~1.2
Grid number (million)	13.7~63.8

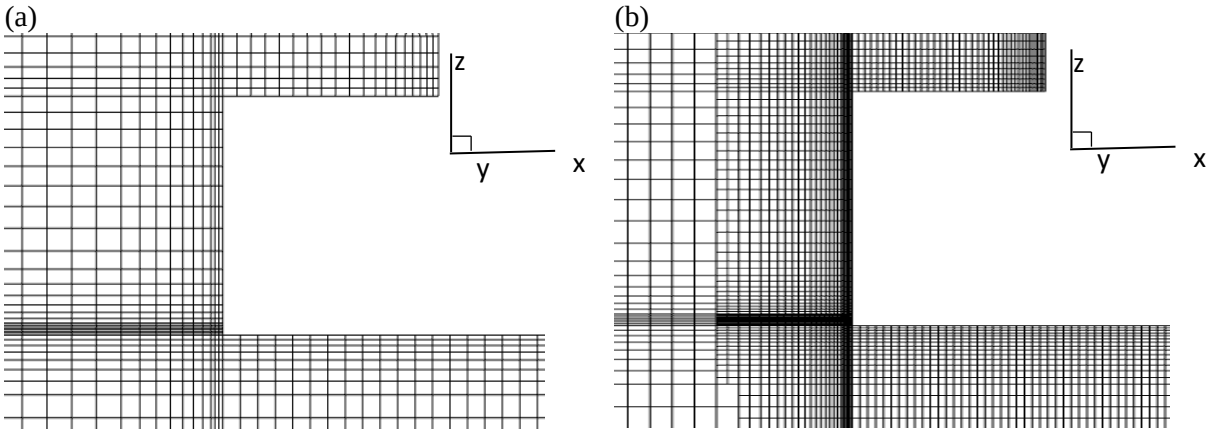

Fig. 3. Local view of mesh around the edge of heave plate HP-1 with (a) grid level 1 and (b) grid level 2 in x-z plane.

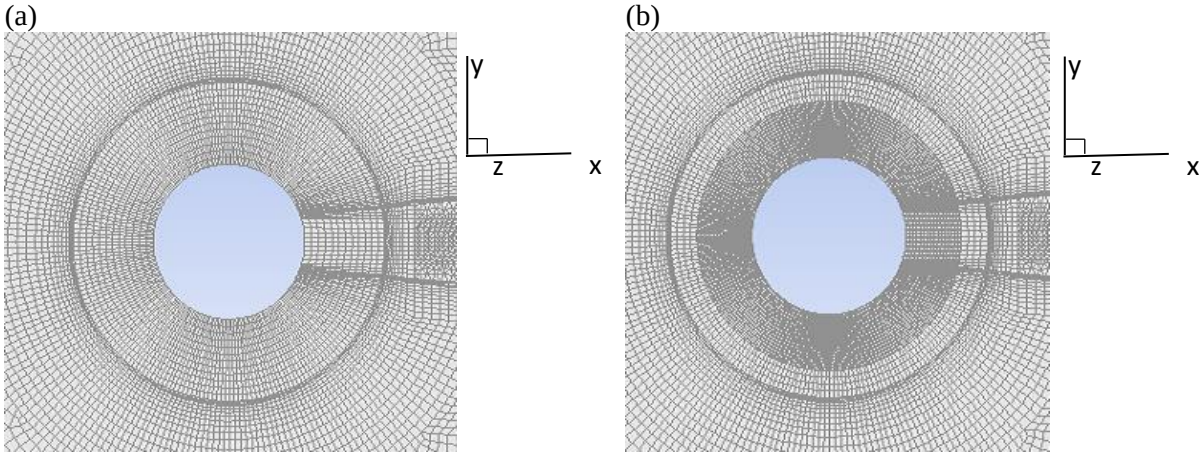

Fig. 4. Local view of mesh for the side column SC-1 with (a) grid level 1 and (b) grid level 2 in x-y plane.

2.4 Numerical schemes and boundary conditions

A finite volume method is employed for present time-dependent numerical simulations shown in the Table 3. A second order central difference scheme is used for the convective and viscous term. A first order implicit scheme is employed for the unsteady term in the momentum equation as shown in Eq.(2), while an explicit approach is adopted for time discretization in the volume fraction equation as shown in Eq.(7). The courant number is 0.25, which means the time step for VOF simulation will be chosen to be one-fourth of the minimum transit time for any cell near the interface. A pressure-based segregated algorithm is used to solve the non-linear and coupled governing equations. A Pressure-Implicit with SIMPLE algorithm is chosen to decrease the iterations for the pressure-velocity coupling solutions as shown the reference [15]. The Table 5 summarizes the numerical schemes used in this study.

The forced vibration tests are carried out in the numerical simulations to evaluate the hydrodynamic coefficients, and dynamic mesh with layering mesh update method is utilized to simulate the movement of the model. The top of air phase and the bottom of water phase are treated as stationary boundaries. Both split and collapse factors for the cells near the boundaries are 0.4 with respect to the first cell height at the boundaries as shown in the reference [10].

Boundary conditions are summarized in Table 6. No-slip wall condition is adopted for the surface of model and bottom of the domain. Symmetry conditions are applied for top and side wells, while the

outflow boundary condition is applied to the inlet and outlet. The static pressure profile in the vertical direction is used to avoid the reflection of water in the horizontal direction.

The governing equations are solved by a software ANSYS Fluent [16]. Near-Wall treatment is used for the wall-adjacent cells. When the mesh is fine enough to resolve the laminar sublayer, the wall shear stress is obtained from the laminar stress-strain relationship. If the mesh is too coarse to resolve the laminar sublayer, it is assumed that the centroid of the wall adjacent cell falls within the logarithmic region of the boundary layer and the law-of-the-wall is employed.

According to the reference [14], five periods of time histories of predicted hydrodynamic force are considered. The predicted hydrodynamic forces are stable enough after the first period as shown in Table 7, The differences between the predicted hydrodynamic coefficients by using the time histories in the last 4, 3 and 2 periods are less than 1%. It means the simulation converges to a stable state after the first period. In order to avoid the effect from the initial unstable solution on the accuracy of hydrodynamic coefficients, the simulated data from the second periods are chosen in the analysis, and the averaged coefficients are used in this study.

Table 5. Summary of numerical schemes.

Items	Scheme
Turbulence model	Smagorinsky-Lilly (C_s =0.032)
Spatial discretization method	Second order central difference scheme
Time discretization for momentum equation	First order implicit scheme
Time discretization for volume fraction equation	Explicit scheme
Pressure-velocity coupling	SIMPLE
Courant number	0.25
Dynamic mesh	Layering

Table 6. Summary of boundary conditions.

Items	Boundary conditions
Model walls	No-slip wall
Top of air phase	Symmetry
Bottom of water phase	Symmetry
Side walls	Symmetry
Inlet and Outlet	Outflow

Table 7. Error estimation for the predicted hydrodynamic coefficients in the horizontally forced vibration with a=0.1m and T=3.0s.

Periods	Mean force	Predicted Ca	Error of Ca	Predicted Cd	Error of Cd
2~5	-0.0116	0.7794	0	1.1106	0
3~5	-0.0083	0.7795	0.01%	1.1123	0.15%
4~5	-0.0092	0.7799	0.06%	1.1141	0.32%

2.5 Definition of hydrodynamic coefficients

The added mass and added inertia moment coefficients matrix, C_a, consists of 36 components for the six degrees of freedom and C_{aij} represents the component in the i^{th} direction due to an unit acceleration in the j^{th} direction. The drag force and drag moment coefficients matrix, C_d, can be similarly defined as C_a.

Due to the symmetry of coefficients matrices, it can be concluded that $C_{aij} = C_{aji}$ and $C_{dij} = C_{dji}$. The surge motion caused by sway, heave and yaw motions induces no transversal force due to

symmetric geometries of floater. and the same consideration can be applied for the heave motion, the added mass and drag force s matrices can be simplified as.

$$[C_a]=\begin{bmatrix} C_{a11} & 0.0 & 0.0 & 0.0 & C_{a15} & 0.0 \\ 0.0 & C_{a22} & 0.0 & C_{a24} & 0.0 & 0.0 \\ 0.0 & 0.0 & C_{a33} & 0.0 & 0.0 & 0.0 \\ 0.0 & C_{a42} & 0.0 & C_{a44} & 0.0 & 0.0 \\ C_{a51} & 0.0 & 0.0 & 0.0 & C_{a55} & 0.0 \\ 0.0 & 0.0 & 0.0 & 0.0 & 0.0 & C_{a66} \end{bmatrix},[C_d]=\begin{bmatrix} C_{d11} & 0.0 & 0.0 & 0.0 & C_{d15} & 0.0 \\ 0.0 & C_{d22} & 0.0 & C_{d24} & 0.0 & 0.0 \\ 0.0 & 0.0 & C_{d33} & 0.0 & 0.0 & 0.0 \\ 0.0 & C_{d42} & 0.0 & C_{d44} & 0.0 & 0.0 \\ C_{d51} & 0.0 & 0.0 & 0.0 & C_{d55} & 0.0 \\ 0.0 & 0.0 & 0.0 & 0.0 & 0.0 & C_{d66} \end{bmatrix} \tag{8}$$

In order to obtain the added mass and drag coefficients of the model. The horizontally and vertically forced vibrations in the numerical simulations are carried out as conducted in the water tank test. The model is forced to oscillate in the horizontal and vertical directions as

$$x(t) = a\ \sin(\omega t) \tag{9}$$

where $\omega = 2\pi / T$ is the frequency of oscillation and a is the amplitude of oscillation as shown in Table 8.

The time series of predicted hydrodynamic force on the wholemodel, $F_H(t)$ by CFD is obtained by subtracting the buoyancy force, F_b, and hydrostatic force, $F_K(t)$, from the total predicted force, $F(t)$, which is obtained from the surface pressure and shear on the model.

$$F_H(t) = F(t) - F_b - F_K(t) \tag{10}$$

$$F_b = \rho_w g \forall \tag{11}$$

where $\forall$ is the displaced volume of water and g is the gravitational acceleration.

The hydrodynamic force on the whole model, $F_H(t)$, can be expressed in the form of Morison's equation as

$$\begin{aligned} F_H(t) &= -C_a\ M\ddot{x}(t) - 0.5\, C_d\ \rho_w\ A\left|\dot{x}(t)\right|\dot{x}(t) \\ &= C_a\ \rho_w \forall a\ \omega^2 \sin(\omega t) - \frac{1}{2} C_d\ \rho_w\ A\,(a\omega)^2 \left|\cos(\omega t)\right|\ \cos(\omega t) \end{aligned} \tag{12}$$

where C_a is the added mass coefficient, C_d is the drag coefficient, $\forall$ and A represent characteristic volume and area according to the definition of C_a and C_d. $\dot{x}(t)$ and $\ddot{x}(t)$ are the velocity and acceleration of the model motion, respectively

As shown in the reference [10], Fourier averages of hydrodynamic coefficients of C_a and C_d are obtained as

$$C_a = \frac{\int_0^T F_H(t)\sin(\omega t)dt}{\rho_w \forall\ a\ \omega^2 \int_0^T \sin^2(\omega t)dt} = \frac{1}{\pi \rho_w \forall\, \omega a} \int_0^T F_H(t)\sin(\omega t)dt \tag{13}$$

$$C_d = -\frac{\int_0^T F_H(t)\cos(\omega t)dt}{\frac{1}{2}\rho_w A(\omega a)^2 \int_0^T \left|\cos(\omega t)\right|\left(\cos(\omega t)\right)\cos^2(\omega t)dt} = -\frac{3}{4\rho_w A \omega a^2} \int_0^T F_H(t)\cos(\omega t)dt \tag{14}$$

2.6 Water tank tests

A water tank test is carried out in this study to validate the predicted C_a and C_d by the numerical simulations. Dimensions of the water tank are 100 m length, 5 m width, and 2.65 m depth. The water

depth in this experiment is set as 2.0 m. Overview of the model is shown in Fig. 5. The detailed dimensions of the semi-submersible model are described in Table 1. The parameters of water tank test are summarized in Table 8.

The time series of measured hydrodynamic force, $F_H(t)$, is obtained by subtracting the buoyancy force, F_b, inertia force, $F_I(t)$, and hydrostatic force, $F_K(t)$, from the measured total force, $F(t)$ as

$$F_H(t) = F(t) - F_b - F_I(t) - F_K(t) \quad (15)$$

$$F_I(t) = -M\,\ddot{x}(t) \quad (16)$$

where M is the model mass including the mass of attachment used to connect the force balance and the model, F_b and $F_K(t)$ are evaluated with the same method used in the numerical simulation.

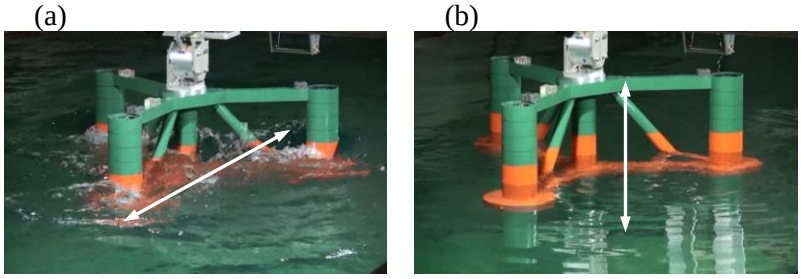

Fig. 5. Overview of the water tank test in (a) horizontally and (b) vertically forced vibrations

Table 8. Parameters and cases used in the forced vibration tests.

Parameters	Symbol	Horizontal	Vertical
Mass of platform (kg)	M	42.2	42.2
Hydrostatic stiffness (N/m)	K_R	-	570.6
Oscillating amplitude (m)	a	0.1, 0.2	0.04, 0.08
KC number	KC	4.62, 9.24	0.9,1.8
Oscillating period (s)	T	1.6~3.0	1.6~3.0
Characteristic area (m^2)	A	0.3216	0.185
Displaced volume of water (m^3)	$\forall$	0.0422	0.0422

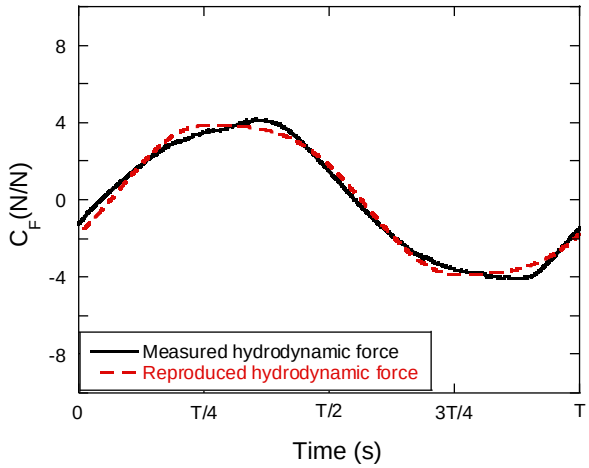

Fig.6. Comparison of measured and reproduced hydrodynamic forces obtained from the water tank test with $a = 0.04\text{m}$ and $T = 1.8\text{s}$ in the vertical direction

The time history of measured and reproduced hydrodynamic force is presented in a non-dimensional form as

$$C_F(t^*) = \frac{F_H(t)}{\frac{1}{2}\rho_w A(\omega a)^2};\ t^* = \frac{t}{T} \tag{17}$$

where, $F_H(t)$ is the measured or reproduced hydrodynamic force; A is the characteristic area in the oscillating direction; and t^* is the non-dimensional time. Fig. 6 shows one example, in which the reproduced hydrodynamic force matches well with the measured force in the water tank test with the oscillating amplitude of 0.04m and the period of 1.8s in the vertical direction.

3. Results and discussions

The hydrodynamic coefficients of a semi-sub floater predicted by grid refinement and Richardson extrapolation are discussed in section 3.1. KC number dependent hydrodynamic coefficients are examined and compared with experiment in section 3.2. The distributed hydrodynamic coefficients considering effect of interaction among each component are presented in section 3.3. The effect of free surface on the hydrodynamic coefficients is investigated in section 3.4.

3.1 Effect of grid refinement

Systematic error estimation for the predicted hydrodynamic coefficients based on the three different grid levels is conducted to obtain a grid independent solution as shown in reference [15]. In this analysis, an approximate solution is obtained by using the fine grid and the grid independent solution is then estimated by Richardson extrapolation. The exact solution Φ and the discretization error ε_h can be expressed as

$$\Phi = \phi_h + \varepsilon_h \tag{18}$$

$$\varepsilon_h \approx \alpha h^p + H \tag{19}$$

where ϕ_h stands for the approximate solution with a grid size of h, H means the higher order terms, α represents the derivative and is independent of h, The exponent p indicates the order of the numerical scheme. The exact solution Φ based on the solution ϕ_{h_i} with the grid size of h_i is then obtained as

$$\Phi = \phi_{h_i} + \alpha h_i^{\,p} + H \tag{20}$$

The exponent p and α are derived by the solutions on the three grid levels as

$$p = \frac{\log\left(\frac{\phi_{h_2} - \phi_{h_1}}{\phi_{h_3} - \phi_{h_2}}\right)}{\log\lambda} \tag{21}$$

$$\alpha = \frac{\phi_{h_3} - \phi_{h_2}}{h_3^{\,p}\left(\lambda^p - 1\right)} \tag{22}$$

where λ means the ratio of grid size, and $h_1 = \lambda h_2 = \lambda^2 h_3$. The discretization error on the third grid can be derived as

$$\varepsilon_{h_3} \approx \frac{\phi_{h_3} - \phi_{h_2}}{\lambda^p - 1} \tag{23}$$

Finally, the exact solution based on the third grid level is obtained as

$$\Phi = \phi_{h_3} + \frac{\phi_{h_3} - \phi_{h_2}}{\lambda^p - 1} \tag{24}$$

Φ can be obtained from the solutions on the two grid levels once the exponent p is obtained .

The predicted Ca and Cd in the case of vertical vibration with the amplitude of 0.04m and the period of 1.8s are presented as one example. The grid is refined as shown in Table 3 and $h_1 = 8mm, h_2 = 4mm, h_3 = 2mm$ represent three different grid sizes respectively. In general, p will be 1 according to the first order scheme of time discretization if the grid velocity is constant. However, p is 0.5 less than 1 since the dynamic mesh with a variable grid velocity is used in this study.

Fig. 7 shows variation of the predicted hydrodynamic coefficients with the grid size. It is found that the predicted drag coefficient based on the grid level 1 is significantly overestimated and the predicted added mass coefficients show relatively weak dependence on grid size. As expected, the error is reduced when the grid is refined, however. the predicted drag coefficient by the finest grid still overestimates that obtained from the water tank test. On the other hand, the predicted drag coefficient by Richardson extrapolation show good agreement with the measurement.

In order to clarify the effect of grid refinement on the hydrodynamic coefficients, instantaneous vorticity is investigated and obtained as

$$w_y = \frac{\partial u}{\partial z} - \frac{\partial v}{\partial x} \tag{25}$$

Fig. 8 illustrates the normalized dynamic pressure obtained from the numerical simulation as shown in the reference [10]. There is no large difference between the dynamic pressures on the two gird levels because the added mass is dominant in hydrodynamic force and is almost independent on the grid level.

Fig. 9 presents a snapshot of the vorticity at t=0 in x-z plane to explain why the prediction error decreases as the grid number increases. The two cases are obtained at t/T=1 when the velocity of plate motion reaches maximum. It can be seen that the vorticity is well captured by the fine grid. The distribution of vorticity is useful to determine the area for the grid refinement near the edge of plate.

The predicted added mass and drag coefficients in the vertically and horizontally forced vibrations are presented in Fig. 10 and Fig. 11. For all the cases, Richardson extrapolation is applied. “Coarse grid” and “Extrapolation” indicate the results obtained by the grid level 1 and Richardson extrapolation. It is found that the drag coefficients in the vertically forced vibration is sensitive to the grid size because the vortex shedding around the edge of plate strongly depends the grid size. The hydrodynamic coefficients predicted by Richardson extrapolation show good agreement with the measurement, however those by the grid level 1 is significantly overestimated in the vertically forced vibration as shown in Fig. 10 (b).

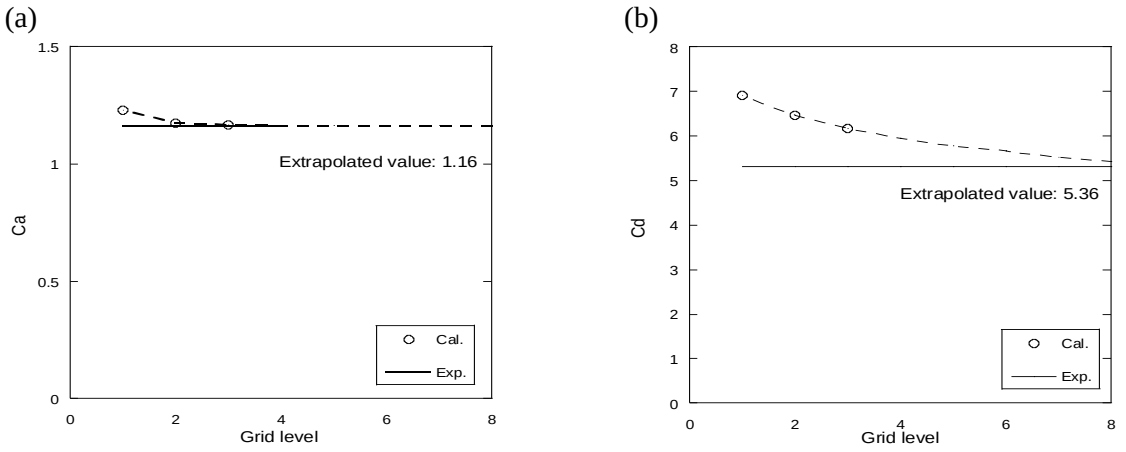

Fig. 7. Variation of the predicted hydrodynamic coefficients of (a) Ca and (b) Cd with the different grid size in the vertically forced vibration with KC=0.9 and *T*=1.8s

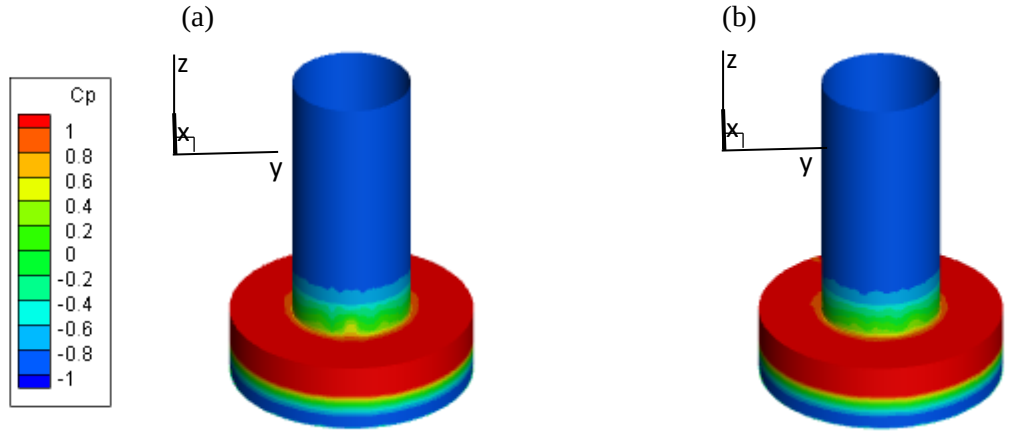

Fig. 8.The normalized dynamic pressure on the surfaces of HP1 and SC1 at t/T=1 calculated with (a) grid level 1 and (b) grid level 2 in the vertically forced vibration with KC=0.9 and T=1.8s

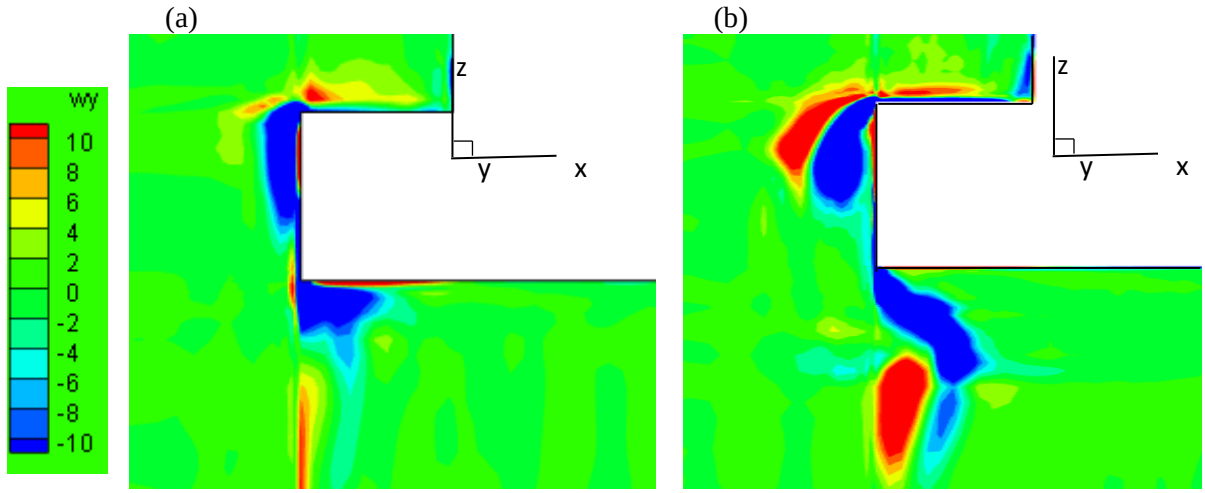

Fig. 9. Instantaneous vortisity around the edge of HP1 at t/T=1 calculated by (a) grid level 1 and (b) grid level 2 for the vertically forced vibration with KC=0.9 and T=1.8s

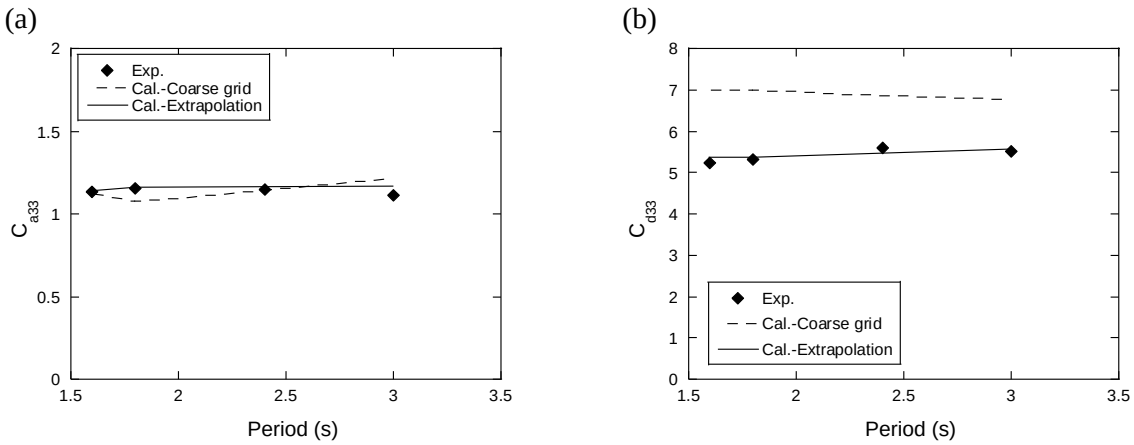

Fig. 10. The hydrodynamic coefficients of (a) Ca and (b) Cd predicted by the grid level 1 and Richardson extrapolation for the vertically forced vibrations with KC=0.9 for the four oscillating periods

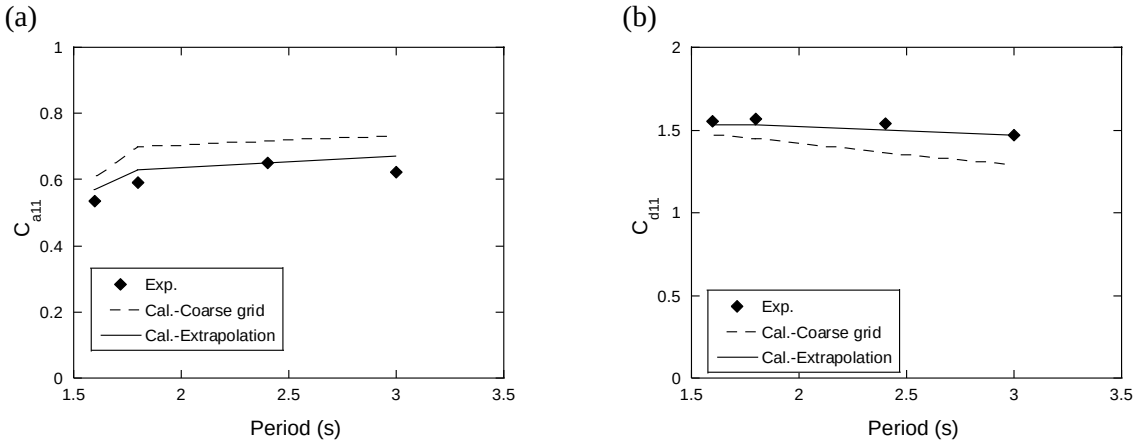

Fig. 11. The hydrodynamic coefficients of (a) C_a and (b) C_d predicted by the grid level 1 and Richardson extrapolation in the horizontally forced vibration with KC=9.24 for the four oscillating periods

3.2 Effect of KC number

The effects of KC number on the hydrodynamic coefficients are discussed for the side column and the whole semi-sub floater. Firstly, the normalized dynamic pressure under the free surface on the side column 2 are shown in Figs. 12 and 13 for the vertical and horizontal vibrations. It is noticed that there is no large difference between the dynamic pressures around the heave plate with different KC numbers for the vertically forced vibration, however, large radiated waves as shown in Fig. 12 (a) are generated near the free surface and result in the change of dynamic pressure on the surface of side column in the horizontally forced vibration.

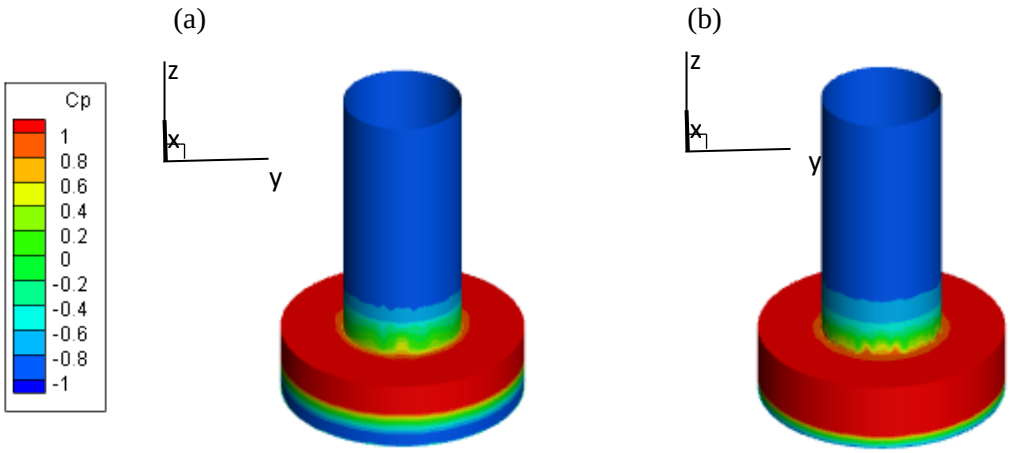

Fig. 12. The normalized dynamic pressure on the surfaces of HP1 and SC1 at *t/T*=1 under the free surface in the vertically forced vibrations with (a) KC=0.9 and (b) KC=1.8

Figs. 14 and 15 show the predicted Ca and Cd in the vertically and horizontally forced vibrations with different periods and amplitudes, respectively. The predicted added mass coefficients by potential theory [16] and the drag coefficients used in the reference [17] are also plotted for comparison. As shown in Fig. 14, Ca and Cd are almost independent on the period, but a function with KC number. It is clear that the added mass coefficients predicted by potential theory is underestimated because the potential theory is based on linear assumption and is only applicable for the small amplitude. The drag coefficients decrease as KC numbers increase. From Fig. 15, it is concluded that the predicted added mass and drag coefficients for the larger oscillating amplitude weakly depend on

the oscillating periods as mentioned in the previous study [8]. In addition, the added mass coefficients decrease as the KC number increases, while the drag coefficients increase as the KC number increases. The predicted hydrodynamic coefficients by CFD well demonstrate KC number dependent characteristics and show favourable agreement with those from the water tank tests.

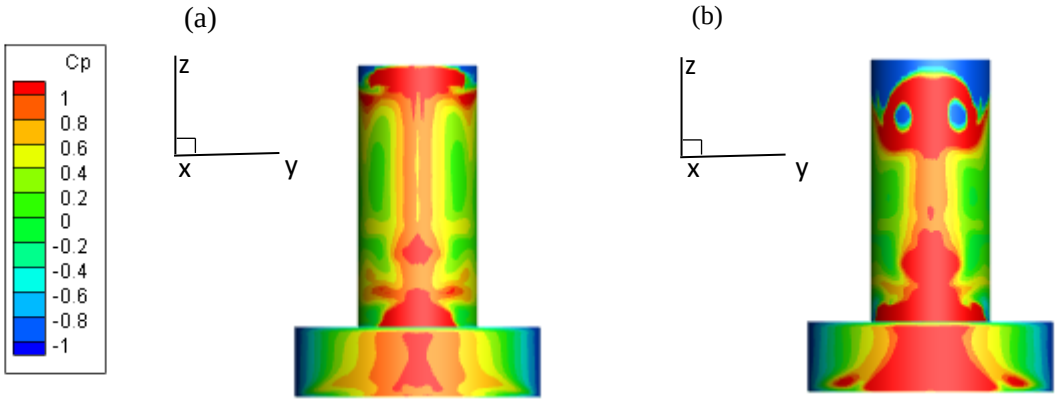

Fig. 13. The nomalized dynamic pressure on the surfaces of HP1 and SC1 at t/T=1 under the free surface in the horizontally forced vibrations with (a) KC=4.62 and (b) KC=9.24

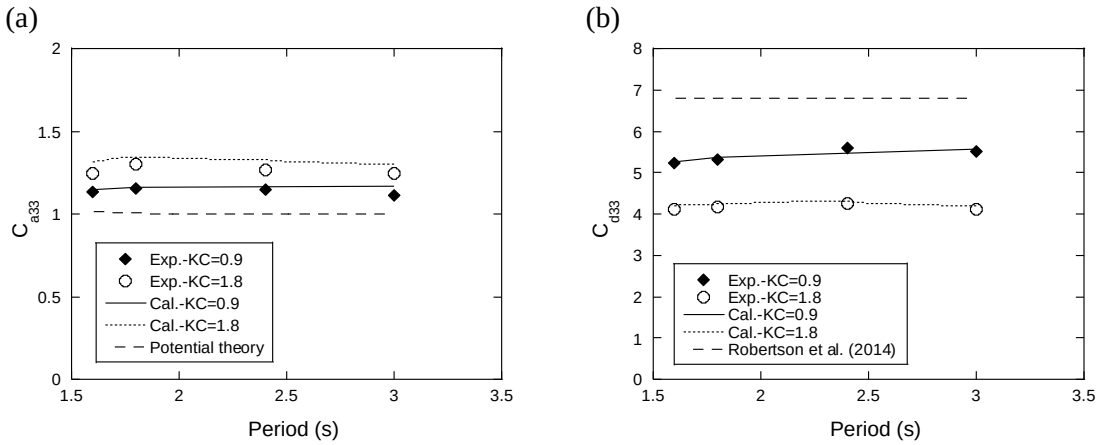

Fig. 14. The predicted hydrodynamic coefficients of (a) C_a and (b) C_d in the vertically forced vibration for two KC numbers and the four oscillating periods.

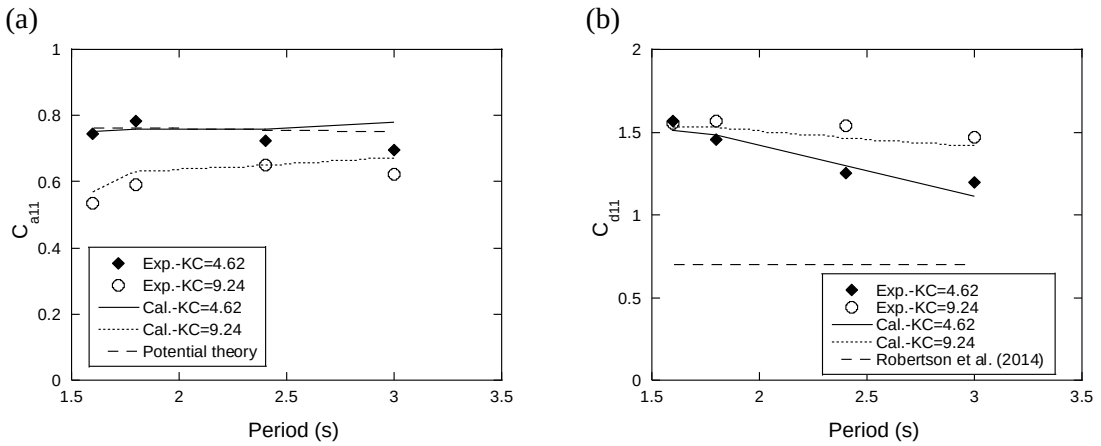

Fig. 15. The predicted of hydrodynamic coefficients of (a) C_a and (b) C_d in the horizontally vibrations for two KC numbers and the four oscillating periods.

The potential theory with the linear assumption accurately predicts Ca with a small oscillating amplitude, but not for the case with a large KC number due to the strong nonlinearity. Besides, the database of Cd provided in the literature [17] did not considered the KC dependency and generally give underestimated predictions. The CFD simulation with VOF not only confirmed the influence of oscillating amplitude (KC number) but also reproduced the oscillating period dependent Ca with a good accuracy. It can be found that the prediction error in terms of Ca and Cd is less than 5% for all cases.

3.3 Effect of interaction between elements

The distribution of hydrodynamic coefficients considering interaction between elements are investigated here. In order to evaluate the distribute hydrodynamic coefficients for each element, the change of the force due to hydrostatic force should be excluded. Special attention should be paid that the area of the lower and upper surface contacted with water is different since the heave plate is attached by one column above. The hydrodynamic force, $F_H(t)$, associating with the Ca and Cd is obtained as

$$F_{Hi}(t) = F_{lower}(t) - \rho_w g h_{lower} A_{lower} + \rho_w g z(t) A_{ower} + F_{upper}(t) + \rho_w g h_{upper} A_{upper} - \rho_w g z(t) A_{upper} \quad (26)$$

where $F_{lower}(t)$ and $F_{lupper}(t)$ are calculated from the instantaneous forces on the lower and upper surfaces of each element. h_{lower} and h_{upper} are the lower and upper surface of each element in the vertical direction when the floater is located at the still water. A_{lower} and A_{upper} are the area of the lower and upper surfaces of each element. $z(t)$ is the instantaneous displacement of the floater .

The distribution of hydrodynamic coefficients for each element are defined as

$$_iC_a^k = \frac{1}{\pi \rho_w \forall_i \omega a_k} \int_0^{T_o} F_{ki}(t) \sin(\omega t) dt \quad (27)$$

$$_iC_d^k = -\frac{3}{4 \rho_w A_i \omega a_k^2} \int_0^{T_o} F_{ki}(t) \cos(\omega t) dt \quad (28)$$

where i expresses the element number, k presents the direction, that is, $k = n$ is in the normal direction and $k = t$ is in the axial direction of element, the characteristic area and volume of each element for normalizing the hydrodynamic coefficients are shown in Table 2. $_iC_a^n$ and $_iC_a^t$ are the added mass coefficients of each element in the normal and axial directions, and $_iC_d^n$ and $_iC_d^t$ refer to drag coefficients of each element in the normal and axial directions, respectively. The hydrodynamic coefficients for each element in the global coordinate can be translated into the local one, then hydrodynamic coefficients predicted by CFD can be directly used for prediction of dynamic response of FOWTs.

The hydrodynamic coefficients for each element in the normal and axial directions are summarized in Table 9. Since the pontoons are rectangular cylinders with variable cross section as shown in Fig. 1, its hydrodynamic coefficients are presented in the horizontal and vertical directions. For instance, the Pntn-1-h and Pntn-1-v represent the values in the horizontal and vertical directions for the Pontoon 1.

The interaction between elements for the predicted hydrodynamic coefficients are also shown in Table 9, where the interaction factor is defined as the ratio of each element to reference element marked by a symbol of *. The hydrodynamic coefficients of SC2 and SC3 are same because there is not any interaction effect and SC2 is chosen as the reference element with the interaction factor of 1. Similarly, SC-2, Hp-2 and Pntn-2 are selected as the reference elements. The hydrodynamic coefficients of SC-1 are smaller than those of SC-2 and SC-3 due to the interaction with the center column. The hydrodynamic coefficients of heave plate Hp-1 and brace Br-1 in the normal direction decrease due the similar reason. It is noticed that though the hydrodynamic coefficient of brace in

normal direction by the horizontally and vertically vibration tests are slight different, the value obtained from the horizontally vibration is adopted in this study.

Table 9. Summary of hydrodynamic coefficients for each element

Element	${}_iC_a^n$	${}_i\gamma_a^n$	${}_iC_d^n$	${}_i\gamma_d^n$	${}_iC_a^t$	${}_i\gamma_a^t$	${}_iC_d^t$	${}_i\gamma_d^t$
Side column SC-1	0.88	0.87	0.49	0.53	0	0	0	0
Side column SC-2 *	1.01	1.00	0.93	1.00	0	0	0	0
Side column SC-3	1.01	1.00	0.93	1.00	0	0	0	0
Center column CC	0.98	-	0.54	-	0	0	0	0
Side heave plate Hp-1	0.33	0.75	0.93	0.62	1.79	1.00	3.09	1.00
Side heave plate Hp-2 *	0.44	1.00	1.50	1.00	1.79	1.00	3.09	1.00
Side heave plate Hp-3	0.44	1.00	1.50	1.00	1.79	1.00	3.09	1.00
Center heave plate Hp-C	0.36	-	1.10	-	2.10	-	3.69	-
Pontoon Pntn-1-h	1.66	1.00	3.28	1.00	0	0	0	0
Pontoon Pntn-2-h *	1.66	1.00	3.28	1.00	0	0	0	0
Pontoon Pntn-3-h	1.66	1.00	3.28	1.00	0	0	0	0
Pontoon Pntn-1-v	1.82	1.00	3.22	1.00	0	0	0	0
Pontoon Pntn-2-v *	1.82	1.00	3.22	1.00	0	0	0	0
Pontoon Pntn-3-v	1.82	1.00	3.22	1.00	0	0	0	0
Brace Br-1	0.75	0.60	0.73	0.42	0	0	0	0
Brace Br-2 *	1.25	1.00	1.73	1.00	0	0	0	0
Brace Br-3	1.25	1.00	1.73	1.00	0	0	0	0
Global value	0.70	-	1.19	-	1.11	--	5.55	-

3.4 Effect of free surface

LES with VOF is employed to consider the effect of free surface on the hydrodynamic coefficients. Multiple phase and the interface between water and air can be described by VOF model. LES model is also used as single phase model, in which only phase of water is considered and the boundary condition of surface is set as symmetry as used in the literature [18].

The normalized dynamic pressure on SC1 and Hp1 under water with and without the effect of free surface in the vertically forced vibration at t/T=1 are revealed in Fig.16. There is no large radiated wave observed during the vertically forced oscillation since the shape of free surface is not disturbed by the vertical columns of the semi-sub platform model and the generated waves are negligible as shown in Fig. 5 (b). It implies that the effect of free surface on the hydrodynamic coefficient in vertical direction can be neglected in the numerical simulation.

However, the shape of free surface around the columns during the horizontally forced vibration changes significantly due to the radiated waves as shown in Fig. 5 (a). The change of dynamic pressure near the free surface is observed in Fig17 (a). It can be seen that some vortices appear near the free surface and lead to the change of dynamic pressure. On the other hand, the change of dynamic pressure is not be observed in Fig17 (b). It implies that accurate prediction of the shape of free surface has great importance for evaluation of the hydrodynamic force on the column since the free surface determines the distribution of the dynamic pressure around the column in the horizontal direction.

Fig. 18 illustrates the predicted Ca and Cd with and without the effect of free surface for several oscillating periods in the vertically forced vibration. It can be seen that the predicted hydrodynamic coefficients with and without the effect of free surface show favourable agreement with those obtained from the water tank tests. This implies that in this condition, CFD without VOF can also be suitable for the hydrodynamic coefficients prediction because the predicted hydrodynamic coefficients keep no change with and without the effect of free surface for a fully submerged heave plate in deep draft. However, the impact of free surface increases as the heave plate is closer to the free surface.

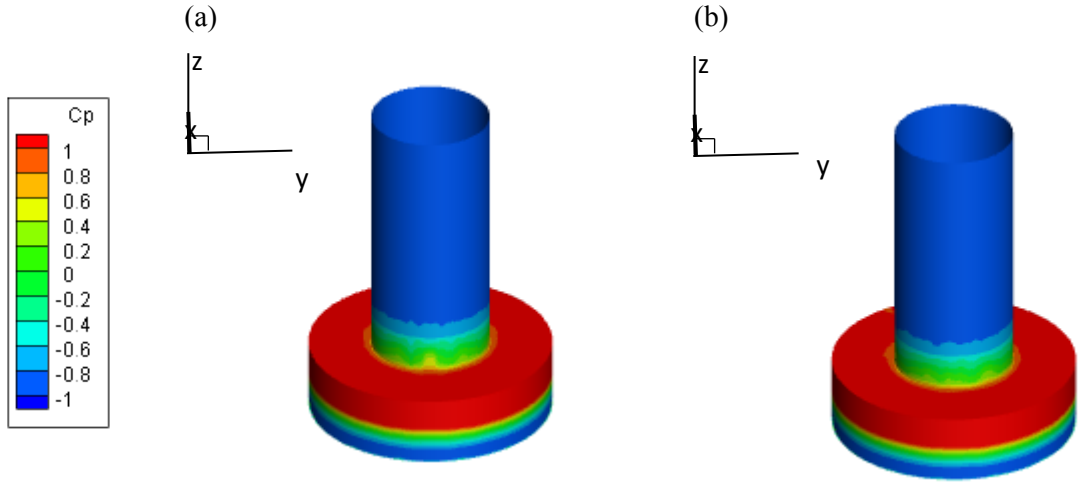

Fig. 16. The normalized dynamic pressure on SC1 and Hp1 under water at t/T=1 (a) with and (b) without the effect of free surface in the vertically forced vibration for KC=1.8 and T=1.8s.

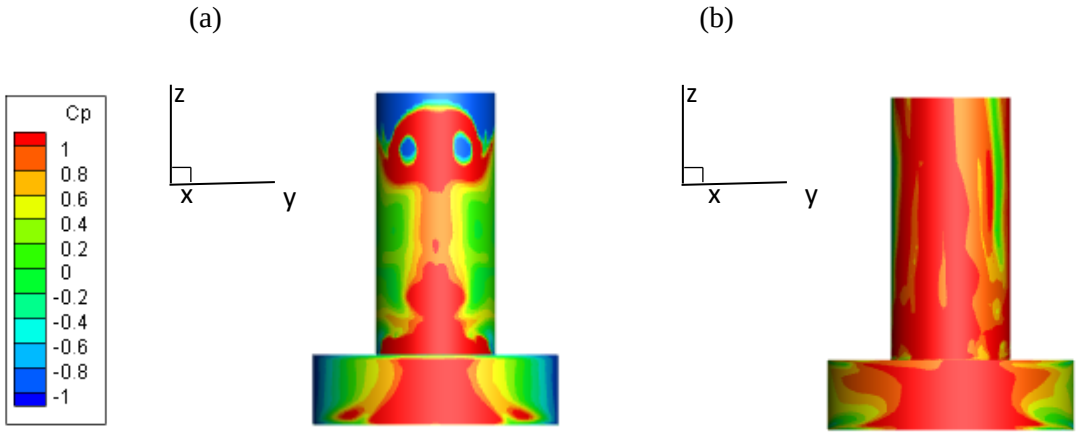

Fig. 17. The normalized dynamic pressure on SC1 and Hp1 under water at t/T=1 (a) with and (b) without the effect of free surface in the horizontally forced vibration for KC=9.24 and T=1.8s

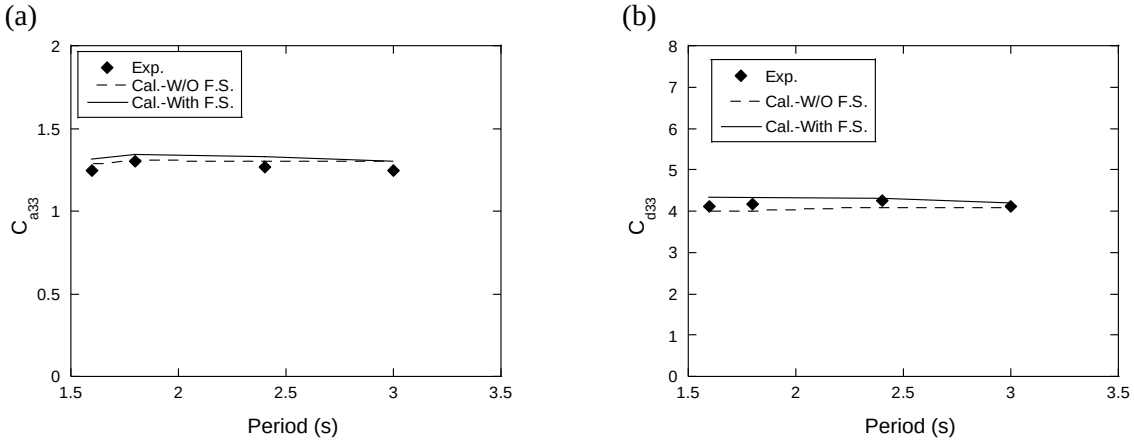

Fig. 18. The predicted hydrodynamic coefficients of (a) C_a and (b) C_d for KC=1.8 in the vertically forced vibration with and without the effect of free surface.

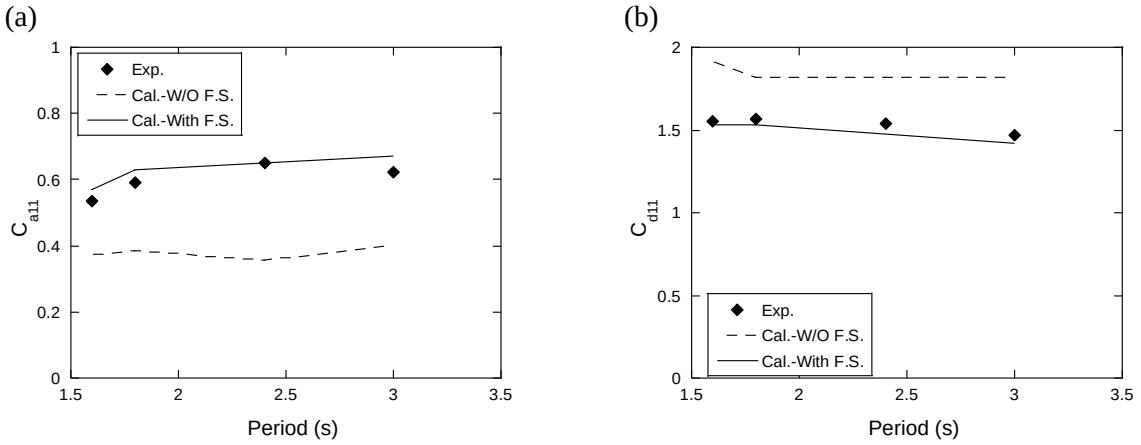

Fig. 19. The predicted hydrodynamic coefficients of (a) C_a and (b) C_d for KC=9.24 in the horizontally forced vibration with and without the effect of free surface.

Fig. 19 shows the predicted Ca and Cd with and without effect of free surface in the horizontally forced vibration. It is obvious that in the simulations without the effect of free surface, the added mass coefficients are underestimated and the drag coefficients are overestimated due to the defect of the predicted hydrodynamic forces on the columns. By contrast, the numerical simulation with consideration of two phase matches well with the measurement. The change of free surface affect both Ca and Cd. This implies that the generated waves induce inertia and radiation damping forces and consideration of the free surface in the numerical simulations is necessary.

4. Conclusions

Numerical studies of hydrodynamic coefficients for a semi-submersible floating offshore wind turbine platform are systematically conducted by using LES with VOF model, and following conclusions are obtained:

1. The grid dependency of predicted hydrodynamic coefficients is observed and the fine grid improves accuracy of prediction because the vortex shedding near the model is captured. The grid independent hydrodynamic coefficients are obtained by Richardson extrapolation and are validated by the water tank tests.
2. The effects of KC number on the added mass and drag coefficients are systematically investigated and the predicted hydrodynamic coefficients by CFD match well with the experimental data, while potential theory underestimates the added mass coefficients in the vertical direction and overestimates that in the horizontal direction for the large KC number.
3. The hydrodynamic coefficients in the normal and axial directions for all the elements of platform are investigated by the vertically and horizontally forced vibrations. The interaction between side and centre columns reduces the added mass and drag coefficients.
4. The effects of free surface on the predicted added mass and drag coefficients are clarified by CFD. In the vertical direction, the hydrodynamic coefficients predicted by LES with and without free surface coincide well with those form the water tank tests since free surface has limited effect in the vertical direction for the deep draft model. However, the hydrodynamic coefficients in the horizontal direction by LES with free surface show a good agreement with the experimental data, while those predicted by LES without free surface show significant discrepancy.

Acknowledgement

This research is carried out as a part of the Fukushima floating offshore wind farm demonstration project funded by the Ministry of Economy, Trade and Industry. The authors wish to express their deepest gratitude to the concerned parties for their assistance during this study.

References

[1] WindFloat: http://www.principlepowerinc.com/en/news-press/press-archive/2016/06/02/principle-powers-windfloat-prototype-celebrates-its-5-year-anniversary-and-the-final-stage-of-technology-demonstration
[2] Fukushima FORWARD: http://www.fukushima-forward.jp/english/index.html
[3] Waris, M.B. and Ishihara, T. "Dynamic response analysis of floating offshore wind turbine with different types of heave plates and mooring systems by using a fully nonlinear model." *Coupled Systems Mechanics*. Vol 1(3): pp. 247-268, 2012
[4] Jonkman, J.M. Dynamics modeling and loads analysis of an offshore floating wind turbine. Technical Report, NREL/TP-500-41958, 2007
[5] Tao, L. and Cai, S. "Heave motion suppression of a Spar with a heave plate." *Ocean Engineering* Vol. 31, No.5, pp: 669-692, 2004
[6] Tao, L., Lim, K. Y. and Thiagarajan, K. "Heave response of classic spar with variable geometry." *Journal of Offshore Mechanics and Arctic Engineering* Vol. 126, No.1, pp: 90-95, 2004
[7] Tao, L., Molin, B., Scolan, Y.-M., and Thiagarajan, K. "Spacing effects on hydrodynamics of heave plates on offshore structures." *Journal of Fluids and Structures*, Vol. 23, No.8, pp: 1119-1136, 2007
[8] Lopez-Pavon, C. and Souto-Iglesias, A.. "Hydrodynamic coefficients and pressure loads on heave plates for semi-submersible floating offshore wind turbines: A comparative analysis using large scale models." *Renewable Energy,* Vol.81, pp: 864-881, 2015
[9] Benitz, M. A., Schmidt, D.P. Lackner, M.A., Stewart, G.M., Jonkman, J. and Robertson, A. Validation of hydrodynamic load models using CFD for the OC4-DeepCwind semisubmersible. *In ASME 2015 34th International Conference on Ocean, Offshore and Arctic Engineering. American Society of Mechanical Engineers*, 2015
[10] Zhang, S., and Ishihara, T. "Numerical study of hydrodynamic coefficients of multiple heave plates by large eddy simulations with volume of fluid method." *Ocean Engineering*, Vol. 163, pp: 583-598, 2018
[11] Klaka, K., Penrose, J.D., Horsley, R.R. and Renilson, M.R. "Hydrodynamic tests on a plate in forced oscillation." *Ocean Engineering*, Vol. 34, No. 8, pp: 1225-1234, 2007
[12] Sarpkaya, T. In-Line And Transverse Forces, On Cylinders In Oscillatory Flow At High Reynolds Numbers. In Offshore Technology Conference. Offshore Technology Conference, 1976
[13] Ishihara, T. and Zhang, S. "Prediction of dynamic response of semi-submersible floating offshore wind turbine using augmented Morison's equation with frequency dependent hydrodynamic coefficients." Renewable Energy, Vol. 131, pp: 1186-1207, 2019.
[14] Oka, S. and T. Ishihara. "Numerical study of aerodynamic characteristics of a square prism in a uniform flow." Journal of Wind Engineering and Industrial Aerodynamics, Vol. 97, pp: 548-559, 2009
[15] Ferziger, J. H. and Peric M. Computational methods for fluid dynamics. Springer Science & Business Media, 2012.
[16] ANSYS, AQWA. "AQWA theory manual." ed. Canonsburg, PA15317, 2013
[17] Robertson, A., Jonkman, J., Musial, W., Vorpahl, F. Popko, W. Offshore code comparison collaboration, continuation: Phase II results of a floating semisubmersible wind system. *EWEA Offshore.* 2013.
[18] Chen, C.R. and Chen, H.C. "Simulation of vortex-induced motions of a deep draft semi-submersible in current" , Ocean Engineering 118, 107-116, 2016.